PHYSICAL REVIEW D **90,** 064020 (2014)

Tidal disruption of a star in the Schwarzschild spacetime: Relativistic effects in the return rate of debris

Roseanne M. Cheng[*,‡] and Tamara Bogdanović[†,‡]

Center for Relativistic Astrophysics, School of Physics, Georgia Institute of Technology, Atlanta, Georgia 30332-0430, USA

(Received 11 July 2014; published 11 September 2014)

Motivated by an improved multiwavelength observational coverage of the transient sky, we investigate the importance of relativistic effects in disruptions of stars by nonspinning black holes (BHs). This paper focuses on calculating the ballistic rate of return of debris to the BH as this rate is commonly assumed to be proportional to the light curve of the event. We simulate the disruption of a low mass main sequence star by BHs of varying masses $(10^5, 10^6, 10^7 M_\odot)$ and of a white dwarf by a $10^5 M_\odot$ BH. Based on the orbital energy as well as angular momentum of the debris, we infer the orbital distribution and estimate the return rate of the debris following the disruption. We find two signatures of relativistic disruptions: a gradual rise as well as a delayed peak in the return rate curves relative to their Newtonian analogs. Assuming that the return rates are proportional to the light curves, we find that relativistic effects are in principle measurable given the cadence and sensitivity of the current transient sky surveys. Accordingly, using a simple model of a relativistic encounter with a Newtonian parametric fit of the peak leads to an overestimate in the BH mass by a factor of ∼few × 0.1 and ∼few in the case of the main sequence star and white dwarf tidal disruptions, respectively.

DOI: 10.1103/PhysRevD.90.064020 PACS numbers: 04.25.Nx, 04.70.Bw, 98.62.Js, 98.62.Mw

I. INTRODUCTION

In a tidal disruption event, a star on a marginally bound orbit disrupts as it reaches a limiting distance of closest approach known as the tidal radius. After disruption one fraction of stellar debris is launched towards the black hole (BH) and remains bound to it, while the remaining fraction is launched away from the BH and unbound. Bound debris forms an accretion disk around the BH and generates the key signature of these events: the tidal disruption flare. Early theoretical models of tidal disruptions predict that the accretion rate onto the BH and consequently the tidal disruption flare, decays with a characteristic time dependence $\propto t^{-5/3}$ [1–3]. This prediction led to the first detections of tidal disruption candidates in the UV and soft x-ray band [4–10] and has been used as a diagnostic for the presence of massive BHs in previously inactive galaxies ever since.

The success of the early theory of tidal disruptions is remarkable, especially given that predictions of the light curve properties are based on the Keplerian return rate of the debris and do not account for the complexities of accretion and radiative processes. Furthermore, subsequent studies have found deviations from the $t^{-5/3}$ falloff for different stellar structure of disrupted stars [11,12]. It has been shown for partially disrupted stars (i.e., close encounters with the BH just outside the tidal radius) that the presence of a self-gravitating remnant core modifies the dynamics of the debris and hence, the accretion rate onto the BH [12]. In this scenario, the released debris elements are deflected from orbits that they would otherwise have in the absence of self-gravitating remnant, resulting in a slope different from $t^{-5/3}$. Similarly, a different dependence is expected for stars disrupted on bound (as opposed to marginally bound, parabolic) orbits [13,14].

An additional layer of complexity in linking the calculated return rate of debris to the observed light curves stems from the fact that the majority of tidal disruption events are expected to result in super-Eddington accretion rates. If these high accretion rates give rise to super-Eddington luminosities, then radiative feedback is also expected to affect the appearance of the tidal disruption light curves [15–19]. Finally, disruptive encounters that occur very close to BHs are subject to relativistic effects, leaving an intriguing possibility that information about the spacetime of a BH is imprinted in the light curve [20–22].

Given the large number of physical processes that play a role in tidal disruption events, it was somewhat fortunate that the early observational campaigns, which relied on a relatively sparse sampling of the light curves, were immune to this level of complexity. Improved multiwavelength observational coverage of the transient sky with GALEX, Swift, Pan-STARRS1, PTF, CRTS, ASAS-SN in the present, and eROSITA, LSST in the future (and the proposed mission ISS-Lobster), are opening a window to study tidal disruption events in unprecedented detail

[*]rcheng@physics.gatech.edu
[†]tamarab@gatech.edu
[‡]Visitor at the Kavli Institute for Theoretical Physics, University of California, Santa Barbara, California 93106-4030, USA.

[23–33]. For the first time high cadence observations in principle permit the measurement of relativistic effects in the light curves of tidal disruptions. This possibility motivates our work on stellar disruptions in the relativistic regime.

In this paper, we investigate the relativistic effects in the return rate of the debris for disruptive encounters between main sequence (MS) stars and BHs of mass $10^5, 10^6, 10^7 M_\odot$. MS-BH encounters are expected to dominate the detection rates and given a large sample of tidal disruption event candidates in the near future, the likelihood of observing relativistic encounters is also higher for this class of events. We also investigate partially disruptive, relativistic encounters between a white dwarf (WD) and a $10^5 M_\odot$ intermediate mass black hole (IMBH) with periastrons very close to the BH. They are important because, if detected, they will uncover the otherwise hidden IMBH population [34–36].

In this paper, we use a hydrodynamics code coupled with self-gravity as well as a general relativistic treatment of the tidal interaction to study the disruption process in the frame of the star [37]. We also develop a series transformation to map quantities in the local frame to the black hole frame. This allows us to characterize the evolution in the distribution of orbital energy and angular momentum of the disrupted star and obtain the ballistic debris return rate onto the BH. We find that relativistic effects are significant and in principle measurable, assuming that the ballistic return rate is proportional to the light curve.

The remainder of this paper is organized as follows: in Sec. II we introduce the parameters of the model and in Sec. III present the method for mapping the debris in the frame of the star and the BH frame. We present the results of the simulations in Sec. IV, discuss their implications in Sec. V and conclude in Sec. VI.

II. PARAMETERS OF THE MODEL

Consider a star of mass M_* and radius R_* in an orbit about a BH of mass M and define the mass ratio as $\mu \equiv M_*/M$. We characterize the strength of the tidal encounter with a parameter η, which compares the hydrodynamical stellar time scale $t_* = (R_*^3/GM_*)^{1/2}$ to the orbital time scale $t_p = (R_p^3/GM)^{1/2}$ at periastron R_p,

$$\eta \equiv t_p/t_* = \left(\frac{R_p^3}{GM}\frac{GM_*}{R_*^3}\right)^{1/2} \tag{2.1}$$

[38]. Disruption occurs for $\eta = 1$ at the tidal radius $R_T \equiv R_* \mu^{-1/3}$. The ratio of stellar radius to periastron in terms of these parameters is $R_*/R_p = \mu^{1/3}\eta^{-2/3}$. Each encounter can also be characterized by a penetration factor $\beta = R_T/R_p = \eta^{-2/3}$. For $\beta > 1$, periastron is less than the tidal radius and the orbital time scale t_p is smaller than the hydrodynamical stellar time scale t_*.

The variation in the specific orbital energy of the released gas depends on the change in the Newtonian BH potential $\Phi(r) = -GM/r$ across the diameter of the star at the tidal radius [1,39]. For a fluid element with orbital velocity $\vec{V}$, the specific orbital energy is $\epsilon_N = \frac{1}{2}V^2 + \Phi(r)$. The spread in ϵ_N across a stationary star in the gravitational potential is $\Delta\epsilon_N = \Phi(R_T - R_*) - \Phi(R_T + R_*)$. Expanding this difference to first order one gets the Newtonian spread in specific energy across the stellar radius at the tidal radius,

$$\Delta\epsilon_N = \frac{GM}{R_T}\frac{R_*}{R_T}. \tag{2.2}$$

For full disruptions, the kinetic energy of the expanding debris is much larger than the adiabatically decreasing internal energy and diminishing self-gravitational energy. By neglecting the self-gravity of the star in this limit, it can be shown that the debris most tightly bound to the BH has orbital energy $\Delta\epsilon_N$. This approximation is valid for deeply penetrating encounters $\beta \gg 1$ ($\eta \ll 1$), where self-gravity is negligible compared to the specific orbital energy at periastron [39]. Thus, for full disruptions, it is reasonable to approximate a "flat" distribution in mass and energy of $dM/d\epsilon \simeq M_*/2\Delta\epsilon_N$ for the debris [3]. Assuming that the debris is locked into Keplerian trajectories after disruption, the semi-major axis of the most tightly bound debris is $a_m = GM/(2\Delta\epsilon_N) = R_p^2/(2R_*)$ with a minimum Keplerian return period of $P_m = (\pi/\sqrt{2GM})R_p^3 R_*^{-3/2}$. The rate at which each debris element returns to its individual periastron after one orbit is

$$\dot{M} = \frac{dM}{d\epsilon}\frac{d\epsilon}{dt} = \frac{1}{3}\frac{M_*}{P_m}\left(\frac{t}{P_m}\right)^{-5/3}, \tag{2.3}$$

where the rate of change of specific orbital energy is $d\epsilon/dt = (1/3)(2\pi GM)^{2/3}t^{-5/3}$. Equation (2.3) shows the canonical form of the rate at which bound debris returns to the BH after one orbit [1–3]. The luminosity L of the flare associated with the accretion disk that forms from the debris is commonly assumed to be proportional to $\dot{M}$ as $L \propto \dot{M}c^2$ (although, see Sec. I for discussion of difficulty in linking the debris return rate to the observed luminosity).

III. NUMERICAL METHOD

The disruption is simulated in a local moving frame known as Fermi normal coordinates (FNC), which follows the star along a parabolic orbit in the known spacetime of a Schwarzschild BH [37]. The central feature of this method is the use of a relativistic tidal field in the vicinity of the trajectory. In the FNC coordinates the tidal field is given by an expansion of the BH spacetime that includes quadrupole and higher multipole moments and relativistic corrections. This approach allows a Newtonian treatment of the self-gravity and hydrodynamics of the star while accounting for

TABLE I. Parameters of initial polytropic models ($n = 1.5, \gamma = 5/3$) for a low mass main sequence star (MS1, MS2, MS3: $M_* = M_\odot$, $R_* = R_\odot$) and a white dwarf (WD: $M_* = 0.6M_\odot$, $R_* = 1.51 \times 10^{-2}R_\odot$). Note $R_* = \mu^{1/3}\eta^{-2/3}R_p$.

Label	η	β	$M[M_\odot]$	$R_p[M]$	R_p[cm]	$\ell_0[M]$	ℓ_0[cm^2 s^{-1}]	$t_p[M]$	t_p[s]	$P_m[M]$	P_m[s]
MS1	1.0	1.0	1.0e + 05	2.2e + 02	3.2e + 12	21.0 (20.9)	9.3e + 21	3.2e + 03	1.6e + 03	2.3e + 06	1.1e + 06
MS2	1.0	1.0	1.0e + 06	4.7e + 01	6.7e + 12	9.9 (9.71)	4.4e + 22	3.2e + 02	1.6e + 03	7.2e + 05	3.5e + 06
MS3	1.0	1.0	1.0e + 07	1.0e + 01	1.5e + 13	5.0 (4.51)	2.2e + 23	3.2e + 01	1.6e + 03	2.3e + 05	1.1e + 07
WD5	1.44	0.784	1.0e + 05	5.0	7.4e + 10	4.1 (3.16)	1.8e + 21	1.1e + 01	5.5e + 00	1.5e + 04	7.2e + 03
WD6	1.89	0.654	1.0e + 05	6.0	8.9e + 10	4.2 (3.46)	1.9e + 21	1.5e + 01	7.2e + 00	2.5e + 04	1.2e + 04

relativistic effects inherent to the BH field. The numerical code, described in [37], provides a high resolution shock capturing calculation of the star as it approaches periastron and follows the debris several dynamical time scales after the tidal accelerations diminish. Quantities in the BH frame are then obtained from the local frame by series transformations given below. In our study, we use the sign conventions and notation of [40], geometrical units in which $c = G = 1$, and scale all dimensional quantities in the simulations relative to the BH mass M. We use Greek indices to label the four-dimensional coordinates and components of tensors of the BH spacetime, latin indices for the FNC frame, and reserve i, j, k, l for FNC spatial coordinates.

A. Frame trajectory and tidal potential

For Newtonian encounters, the frame is evolved along a parametrized parabolic orbit given in [41]. We use a tidal potential derived from the multipole expansion of the Newtonian gravitational potential $\Phi(r)$ for the BH. The local frame is located at a distance $\vec{R}_0$ from the BH. The expansion of Φ at a distance $\vec{x}$ from the origin of the local frame is

$$\Phi = -\frac{GM}{R_0} + \frac{GM}{R_0^2}\vec{x}\cdot\vec{n} + \frac{1}{2}C_{ij}x^ix^j + \frac{1}{6}C_{ijk}x^ix^jx^k + \frac{1}{24}C_{ijkl}x^ix^jx^kx^l + \cdots, \tag{3.1}$$

where $\vec{n} = \vec{x}/R_0$, with tidal tensor definitions $C_{ij} \equiv (\partial_i\partial_j\Phi)_0$ (quadrupole), $C_{ijk} \equiv (\partial_i\partial_j\partial_k\Phi)_0$ (octupole), $C_{ijkl} \equiv (\partial_i\partial_j\partial_k\partial_l\Phi)_0$ (hexadecapole), etc., which depend on the evolution of the local frame center along the trajectory. The gravitational acceleration due to the BH in this local frame is $\partial_i\Phi$, where the first term is the frame acceleration and subsequent terms are the tidal accelerations. The tidal potential is then defined as

$$\Phi_{\rm tidal} = \frac{1}{2}C_{ij}x^ix^j + \frac{1}{6}C_{ijk}x^ix^jx^k + \frac{1}{24}C_{ijkl}x^ix^jx^kx^l + \cdots. \tag{3.2}$$

We apply only the tidal accelerations $\partial_i\Phi_{\rm tidal}$ to the self-gravitating star in the local frame. For relativistic encounters, the frame is evolved along a trajectory in the Schwarzschild spacetime with parametrization given in [42]. We use a tidal potential as in Eq. (3.2), derived from the formalism of [37,43], with tidal tensors $C_{ij} \equiv R_{0i0j}$, $C_{ijk} \equiv R_{0(i|0|j;k)}$, and $C_{ijkl} \equiv R_{0(i|0|j;kl)}$ defined by the FNC Riemann tensor R_{abcd} and its derivatives with respect to FNC spatial coordinates.

B. Validity of the FNC approximation

In the following, we show the validity of the FNC approximation g_{ab} of the BH spacetime $g_{\mu\nu}$ for all encounters in this paper (listed below in Table I) [37]. In order for this approximation to be valid the size of the computational domain must be smaller than the characteristic length scale of the tidal field, which is smallest at periastron R_p. In this study, the extent of the computational domain is $\mathcal{L} = 16R_*$ and we have $\mathcal{L}/R_p \ll 1$ for all encounters. The correction due to the motion of the BH (relative error of $\sim\mu$, where the largest mass ratio is $\mu \sim 10^{-5}$) is neglected. We account for the error in neglecting terms higher than the hexadecapole term in the metric expansion as well as the gravitomagnetic term. We consider stars that have stellar post-Newtonian (PN) velocity scale $\varepsilon^2 = GM_*/(c^2R_*) \ll 1$. Comparing the leading neglected term higher than the hexadecapole with the Newtonian quadrupole, which is the dominant force term, we obtain a fractional error in neglecting higher order quartic tidal terms at a stellar radius R_* from the origin of the FNC frame,

$$\mathcal{E}_{\rm quartic} \simeq \frac{M}{R_p^3}R_*^2 = \varepsilon^2\eta^{-2}. \tag{3.3}$$

We consider the error in neglecting the gravitomagnetic potential by comparing the leading term in g_{0m} multiplied by the maximum break-up velocity for the star ε with the size of the Newtonian quadrupole and obtain

$$\mathcal{E}_{\rm GM,max} \simeq \varepsilon^2\mu^{-1/3}\eta^{-1/3}. \tag{3.4}$$

We find that the fractional error in neglecting terms above the hexadecapole term is at most $\mathcal{E}_{\rm quartic} \sim 10^{-5}$ for main sequence stars and white dwarfs. The fractional error in neglecting the gravitomagnetic term is at most $\mathcal{E}_{\rm GM,max} \sim 10^{-4}$ for the main sequence star models and $\sim 10^{-3}$ for the white dwarf model. Given the low level of error associated with the higher order terms in the FNC expansion, we

assume that they can be safely neglected for all parameter choices in this study.

C. Transformation from local to BH frame

We transform quantities calculated in the local frame to the black hole frame in order to obtain the orbital parameters of the debris. For the Newtonian case, this is a straightforward Galilean transformation. For the relativistic case, quantities corresponding to an event $x^a = (\tau, x^i)$ in the FNC frame are transformed to the BH frame at coordinate location X^μ by series expansion about the origin of the local moving frame, $X^\mu_{(0)}$. This is possible because the positions and velocities of the fluid elements in the local frame are smaller than the position and motion of the frame with respect to the BH. For the fluid velocities considered in this paper, we include more terms in the expansion than [37]. For the coordinate transformation, we form a Taylor expansion in the spatial coordinates x^i,

$$X^\mu(\tau, x^i) = X^\mu_{(0)}(\tau) + \lambda_i{}^\mu x^i + \frac{1}{2}\sigma_{ij}{}^\mu x^i x^j + \frac{1}{6}\kappa_{ijk} x^i x^j x^k + \cdots, \tag{3.5}$$

where the coefficients $\lambda_i{}^\mu$, $\sigma_{ij}{}^\mu$, and $\kappa_{ijk}{}^\mu$ are evaluated at $X^\mu_{(0)}$. For the velocity transformation, we expand about the frame center in both spatial coordinates x^i and velocities v^i. We write the four-velocity in the BH frame as $U^\mu = dX^\mu/d\tau = (\partial X^\mu/\partial\tau)u^0 + (\partial X^\mu/\partial x^i)u^i$, where in the FNC frame the four-velocity reduces to $u^0 \simeq 1 + \mathcal{O}(\varepsilon^2)$ and $u^i = v^i + \mathcal{O}(\varepsilon^3)$ in neglecting corrections at or below the size of the stellar PN order ε^2. Expanding X^μ, we have

$$U^\mu(\tau, x^i, v^i) = U^\mu_{(0)} + \left(\frac{d}{d\tau}\lambda_i{}^\mu\right)x^i + \frac{1}{2}\left(\frac{d}{d\tau}\sigma_{ij}{}^\mu\right)x^i x^j + \frac{1}{6}\left(\frac{d}{d\tau}\kappa_{ijk}{}^\mu\right)x^i x^j x^k \lambda_i{}^\mu v^i + \sigma_{ij}{}^\mu v^i x^j + \frac{1}{2}\kappa_{ijk}{}^\mu v^i x^j x^k + \cdots, \tag{3.6}$$

with coefficients evaluated at $X^\mu_{(0)}$. We have that $\lambda_i{}^\mu$ is the FNC tetrad [37] and obtain $\sigma_{ij}{}^\mu$ and $\kappa_{ijk}{}^\mu$ in terms of the connection coefficients $\Gamma^\mu{}_{\alpha\beta}$ of the BH spacetime in Appendix A. For the encounters in this paper, higher order terms (than those mentioned above) in the expansion are smaller than the overall relative error in the numerical method, $\mathcal{E} \lesssim 10^{-3}$ (see Sec. III B), and are neglected. Using the position X^μ and velocity U^μ of a debris element in the BH frame, we calculate the orbital parameters represented by specific orbital energy ϵ and specific orbital angular momentum ℓ (or alternatively periastron distance R_p and eccentricity e). We outline this calculation in Appendix B.

IV. RESULTS

A. Initial setup

In this paper, we consider $n = 3/2$ polytropes with $\gamma = 5/3$ adiabatic index for modeling a low mass main sequence star (MS1, MS2, MS3: $M_* = M_\odot$, $R_* = R_\odot$) and a white dwarf (WD5, WD6: $M_* = 0.6M_\odot$, $R_* = 1.51 \times 10^{-2}R_\odot$). We simulate $\sim 20t_p$ before and $\sim 40t_p$ after periastron passage. In Table I, we give the parameters for the initial models simulated in this paper in units of geometrized BH mass M and CGS units. We give encounter strength η in Eq. (2.1), the corresponding penetration factor β, mass of the BH M, periastron R_p, relativistic specific angular momentum of the frame trajectory (Newtonian quantity in parentheses) ℓ_0, orbital time scale at periastron t_p, and estimated Keplerian return period of the most bound debris P_m in Eq. (2.3).

The star is centered in a computational domain of length $\mathcal{L} = 16R_*$ in order to follow the evolution of the remnant core and tidal debris streams as the stellar fluid expands in the encounter. Each simulation is modeled using a uniform grid with a resolution of 32 zones per stellar radius R_*. The numerical accuracy in computing the energy and angular momentum deposited onto the star with this code at different resolutions is discussed in [37]. In particular, convergence is shown in simulations of tidally transferred energy (Fig. 6) with angular momentum conservation (Fig. 15). Resolution higher than 32 zones per radius is necessary for weak tidal encounters $\eta = 4$. For encounters with greater energy and angular momentum transfer $\eta \gtrsim 2$, convergence is achieved with lower levels of resolution. In this paper, we model encounters of strength $\eta \sim 1$, at the threshold of disruption.

B. Orbital dynamics of the debris

Orbital dynamics of the debris in the BH frame is characterized by ϵ and ℓ. The left and center panel of Fig. 1 show the normalized change in specific orbital energy ϵ and angular momentum ℓ of the debris, respectively, at $1.5t_p$ after periastron passage. We normalize the distribution in specific orbital energy as $\delta\bar{\epsilon} = (\epsilon - \epsilon_0)/|\epsilon|$, where $\epsilon_0 = 0$ (or $\epsilon_0 = 1$ for the relativistic case) is the specific orbital energy of the trajectory of the frame. Similarly, the normalized distribution in specific angular momentum is calculated as $\delta\bar{\ell} = (\ell - \ell_0)/\ell_0$, where ℓ_0 is the specific orbital angular momentum of the initial trajectory of the frame. The left and center panel of Fig. 1 show that the tidal lobe bound to the BH has less angular momentum than the initial trajectory as well as a gradient in the distribution of angular momentum. This implies that the expanding debris will eventually occupy a range of orbits with different semi-major axes and eccentricities.

The right panel of Fig. 1 is a contour plot of the Mach number $\mathcal{M} = |\vec{v}|/c_s$ for the locally defined fluid velocity $\vec{v}$

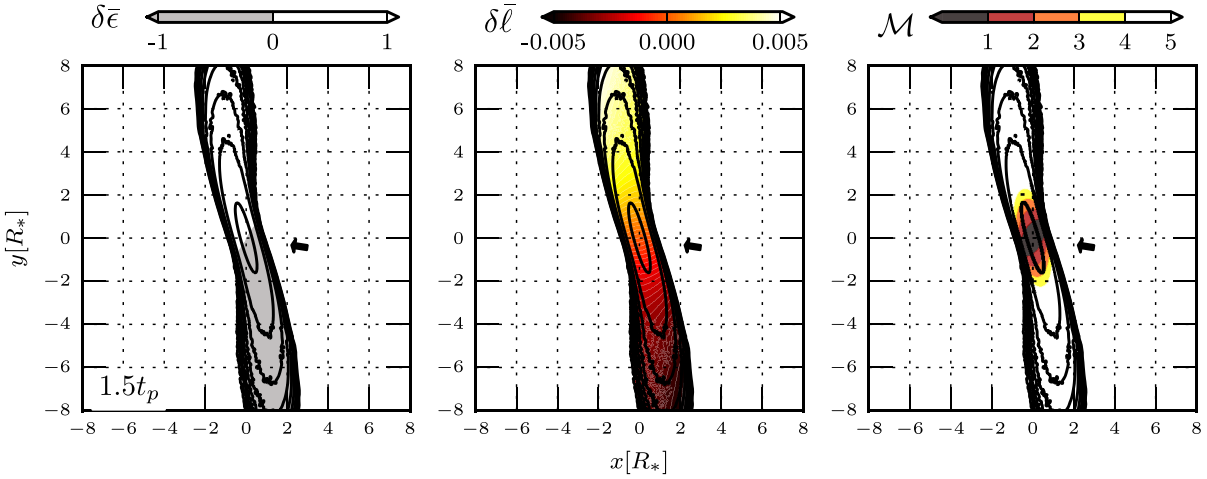

FIG. 1 (color online). Normalized distribution of the specific orbital energy ϵ (left), specific orbital angular momentum ℓ (middle), and the Mach number $\mathcal{M}$ (right panel) of the debris at $1.5t_p$ after the periastron passage for relativistic model MS3. The density contours (black lines) are of $\log_{10}(\rho/\rho_c)$, ranging from -5 to 0 in steps of 0.5, where ρ_c is the initial central density of the star. Arrow indicates the direction from the BH to the star.

and sound speed c_s. The remnant core of the star is subsonic $\mathcal{M} < 1$ and the two tidal debris streams are supersonic, in agreement with the findings of [44]. We track the tidal lobes as they escape the domain and include the supersonic material (which is no longer causally connected to the remnant core hydrodynamically) in our estimate of the orbital parameters of the debris.

C. Distribution of specific orbital energy and angular momentum

We construct the maps of the distribution of ϵ and ℓ of the debris for all tidal encounters studied in this paper and investigate their evolution with BH mass and stellar type. In Fig. 2, ϵ and ℓ are given at the end of Newtonian and relativistic simulations of models MS1, MS2, and MS3. The contour levels indicate the enclosed fraction of the debris mass, $\Delta M/M_*$. In this figure, the change in specific orbital energy is normalized by the Newtonian spread in energy $\Delta\epsilon_N$ in Eq. (2.2) and the normalized change in specific orbital angular momentum is the same as Fig. 1. In Fig. 2, the spread in ℓ decreases with the BH mass for both the Newtonian and relativistic simulations. The spread in ϵ is similar for both and larger than $2\Delta\epsilon_N$, indicating a full disruption of the star.

Comparing the Newtonian and relativistic simulations in Fig. 2, we find a further decrease in the width of the ℓ distribution for relativistic cases relative to their Newtonian

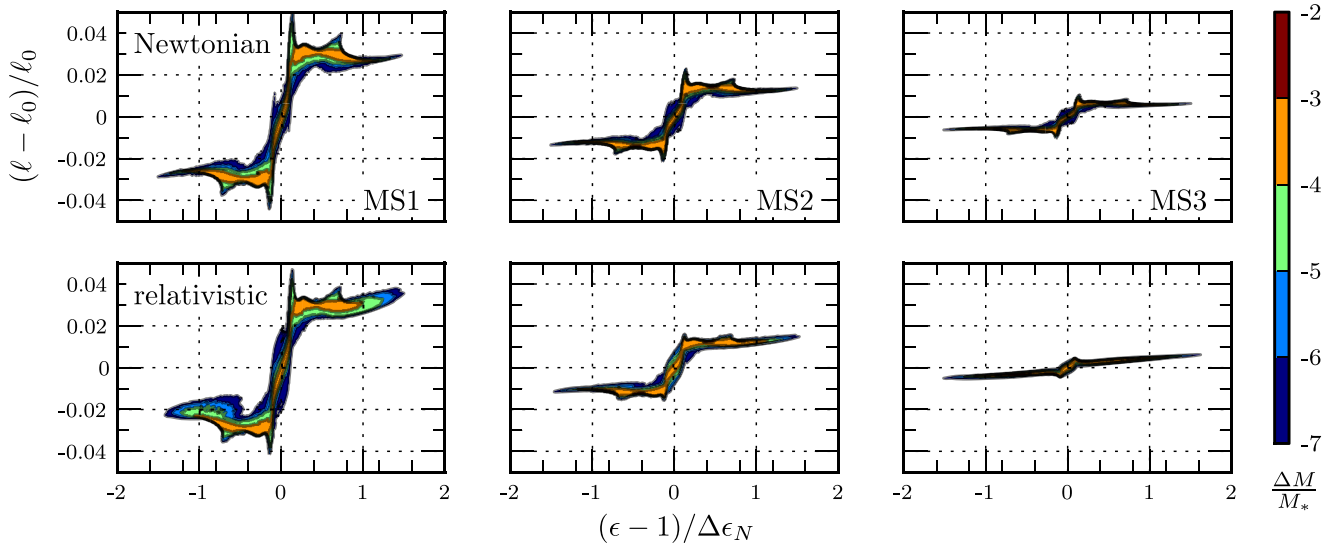

FIG. 2 (color online). Distribution of specific orbital energy and angular momentum of the debris at the end of the encounter for Newtonian and relativistic models MS1, MS2, and MS3. Color indicates the stellar mass fraction enclosed in every contour level.

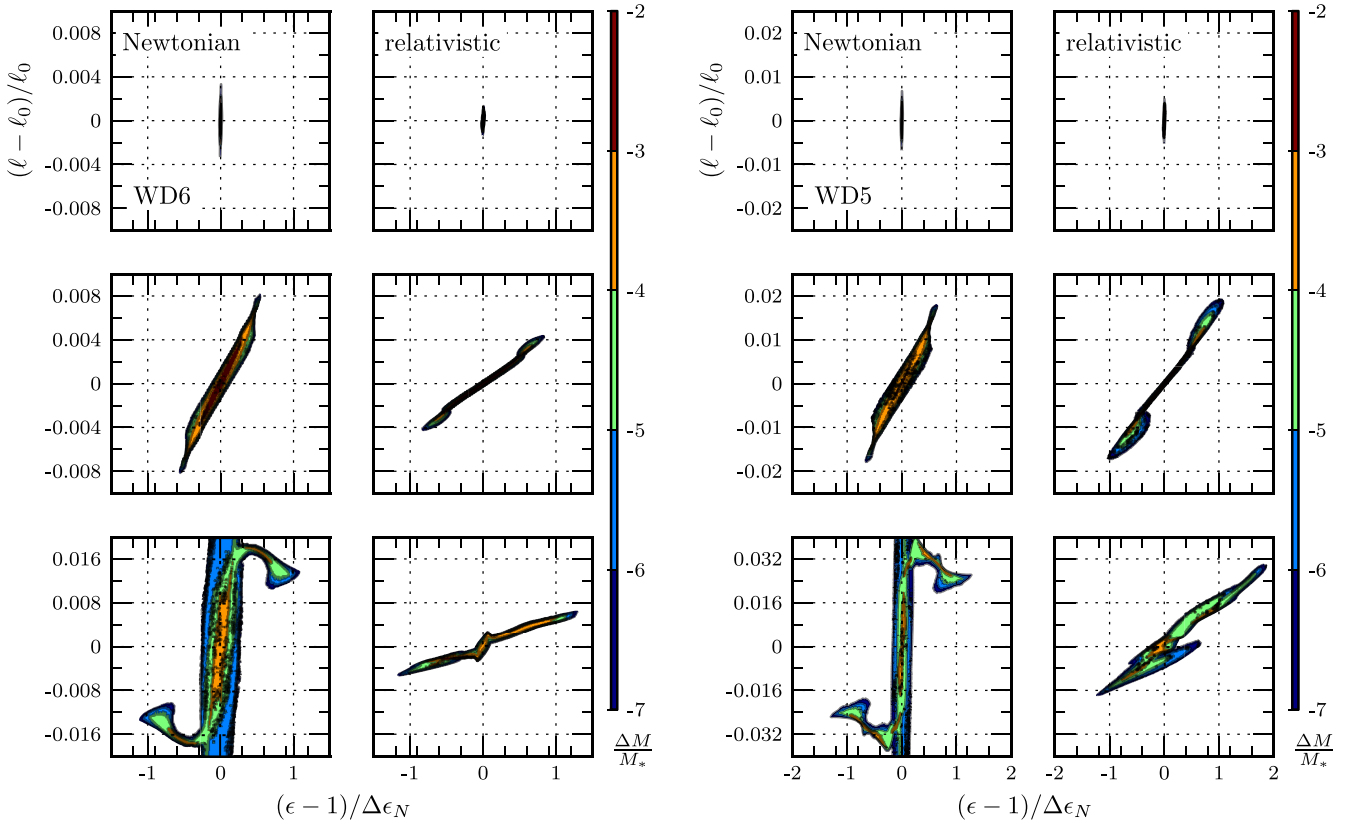

FIG. 3 (color online). Distribution of specific orbital energy and angular momentum of the debris for Newtonian and relativistic model WD6 (left) and model WD5 (right) at different points in the encounter: initially (top row), periastron (middle row), end of encounter (bottom row).

counterparts. This effect is even more pronounced in models WD6 and WD5, shown in the bottom rows of Fig. 3. The narrowing of the angular momentum distribution in relativistic simulations for models MS3, WD5 and WD6 indicates that in these simulations debris is confined to a narrower range of eccentric orbits. Since only the $\epsilon < 0$ branch remains bound to the BH, for which $\delta\bar{\ell} \lesssim 0$, it follows that all bound orbits will be highly eccentric relative to the initial orbit of the incoming star and that the Newtonian simulations give rise to more eccentric debris orbits than relativistic ones. As relativistic simulations are similar to their Newtonian equivalents in every aspect except in the relativistic treatment of the tidal interaction with the BH, it follows that this effect is purely relativistic.

In Fig. 3, we show the evolution of the $\epsilon - \ell$ distribution with time for WD6 and WD5 (nominally $\eta = 1.89$ and 1.44 encounters, respectively) at the beginning of the encounter (top row), periastron (middle row), and the end of the encounter (bottom row). For both the Newtonian and relativistic simulations, the distribution in ϵ and ℓ initially broadens as the star passes through periastron.

In Newtonian simulations, the distribution in energy after periastron passage evolves to become more "vertical." This is an indication of the diminishing tidal accelerations and increasing significance of the self-gravity of the stellar remnant, which in this case was not fully disrupted as it continues to recede from the BH. This effect is also seen in simulations of disruptions by [11–13] and is manifested as a central spike in their one-dimensional plots of the distribution of mass and energy $dM/d\epsilon$. Note that similar one-dimensional distributions can be obtained from our $\epsilon - \ell$ maps by summing along the angular momentum (vertical) axis.

After periastron passage, the distribution in orbital energy of the debris is wider in relativistic simulations. Unlike in the Newtonian simulations, the spread in energy at periastron in relativistic simulations indicates full disruption. This is consistent with findings of [20,44], who note that differences between the relativistic and Newtonian tidal tensor imply that the relativistic tidal interactions are more disruptive.

An additional feature of the $\epsilon - \ell$ maps, noticeable in the most relativistic encounter WD5 (Fig. 3), is that the symmetry in the distribution of the debris breaks down after periastron passage (bottom right panel). Specifically, the tidal lobe bound to the BH evolves to be less strongly bound than it would otherwise be if the symmetry in the distribution was preserved as in the WD6 model. We show this to be a consequence of apsidal precession in the next

section, where we describe the dynamics of the debris streams in the black hole frame.

Using the orbital parameters of the debris calculated from the maps of ϵ and ℓ (shown in Figs. 2 and 3), we construct *ballistic debris elements* from a collection of fluid elements that share similar values in ϵ and ℓ. We then propagate them ballistically in time according to the procedures for the Newtonian and Schwarzschild spacetimes described in Appendix B.

D. Whirling debris streams in the black hole frame

In this section, we report a mixing of bound and unbound streams for the most relativistic encounter WD5. In a Newtonian simulation, the debris streams should be distinct (opposite sides of the remnant core) with roughly 50% of the debris bound to the black hole. For the relativistic WD5 encounter, we find that 45% of the debris is bound to the black hole. In Fig. 4, we show the evolution of the ballistic debris elements in the relativistic run WD5. We also denote the location of a test particle that follows the initial orbit of the star. In this plot, the black debris stream represents material bound to the BH while the red debris stream is unbound. In this encounter the apsidal precession shapes the distribution of the debris and the result is a whirling, crescent shaped tidal tail where bound and unbound material overlap and mix. The same effects are present in the run WD6 to a lesser extent. This distribution and mixing of the bound and unbound debris share resemblance with the relativistic MS-BH disruptions by [45] as well as neutron star-BH disruptions by [46–50]. They indicate that the orbital precession is likely to lead to orbit intersection and collisions of fluid elements as they pass through the periastron. This differs from the Newtonian encounters, where the initial orbital trajectory clearly delineates the bound and unbound debris streams. We caution that we evolve the debris ballistically and therefore do not account for hydrodynamic interactions and self-gravity. This approximation ceases to be valid once the orbits of the fluid elements intersect. Therefore, a full hydrodynamic treatment is necessary in order to follow the evolution of the debris accretion disk.

E. Apsidal advance in the debris orbits

In order to investigate the relativistic effects which result in an apsidal advance of the debris orbits, we map the periastron locations of the debris in azimuthal angle (ϕ_p) and radius (R_p) for both Newtonian and relativistic simulations (Fig. 5). Both sets of simulations show that the

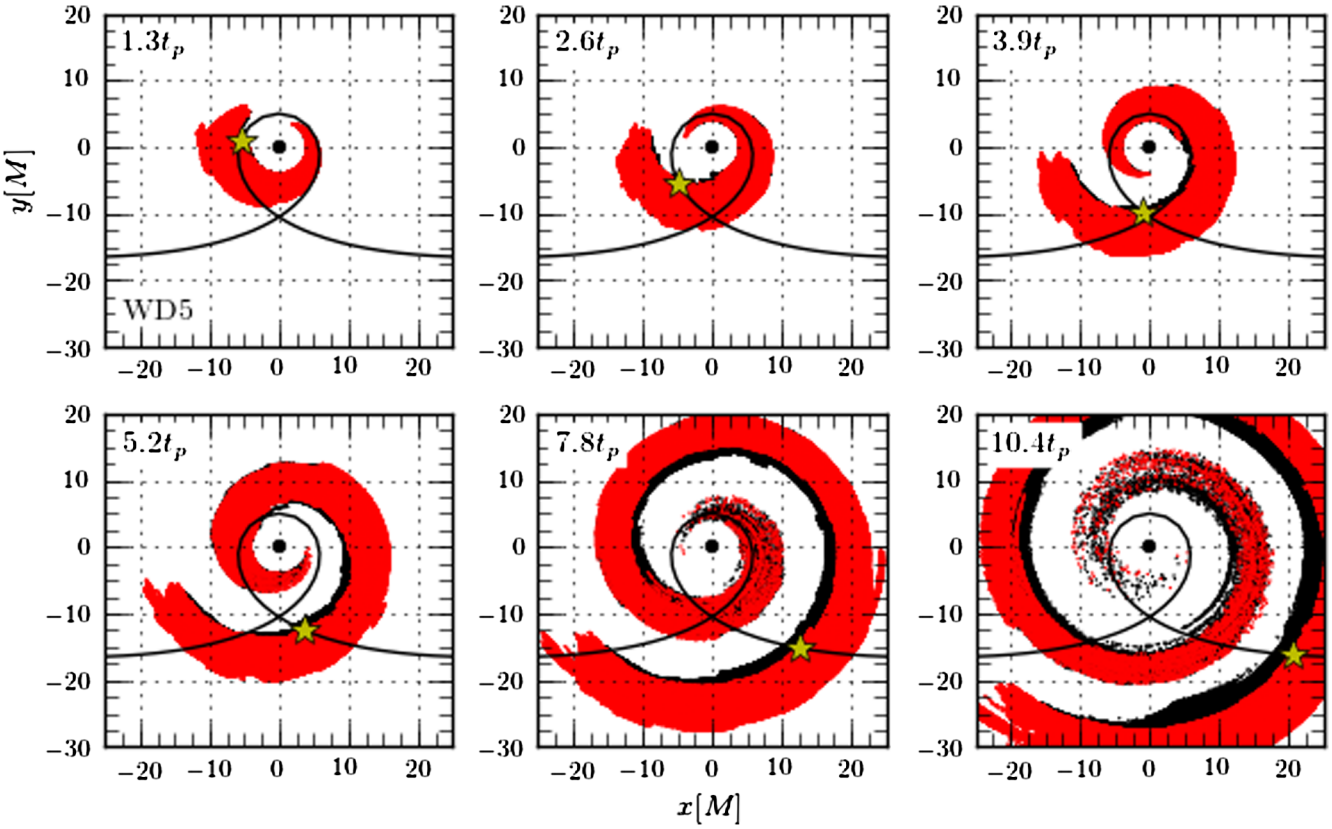

FIG. 4 (color online). Debris streams in the BH frame for relativistic model WD5. Black (red) color marks a portion of the debris stream bound (unbound) to the BH. Note that the streams are overlapping with 45% of the debris bound to the black hole. Star marker follows the initial trajectory of the star.

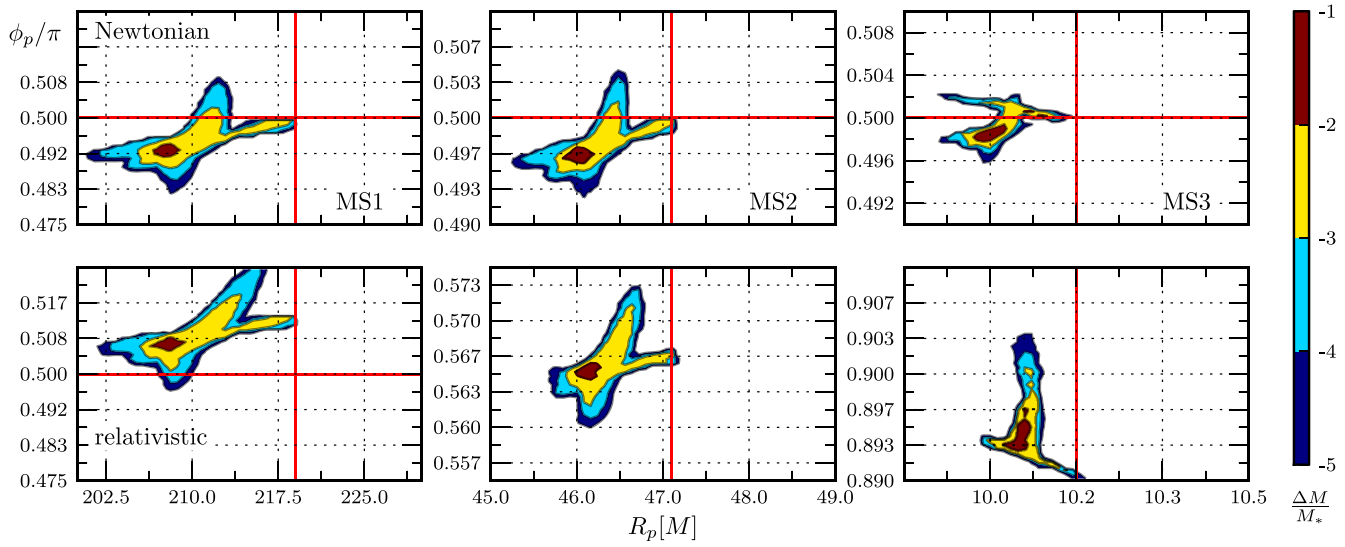

FIG. 5 (color online). Periastron location of the debris for Newtonian and relativistic simulations MS1, MS2, and MS3. Periastron location of the initial orbit is indicated by the cross hairs.

debris returns to the periastron radii that are slightly smaller than that of the original orbit (indicated by the vertical red line). They however exhibit different behaviors when it comes to the distribution of the debris in the azimuthal angle.

In Newtonian simulations, following the disruption, the bulk of the debris returns to the periastron in $\lesssim 2\pi$ azimuthal rotation relative to the initial periastron located at $\pi/2$. This can be understood in terms of the tidal interaction between a star and a BH. If the disruption of a star occurred instantaneously at periastron, the debris would return to this point on the orbit in a full 2π azimuthal rotation. In reality however, the star is starting to be tidally deformed and spun up before it reaches periastron and consequently, its fluid elements start acquiring a range of values in angular momentum. The effect of azimuthal offset in Newtonian simulations decreases with the BH mass; it is strongest in the MS1 and weakest in the MS3 run (see Fig. 6 for illustration of the periastron locations for the bulk of the stellar debris in different simulations). Note that this is consistent with the narrowing in the angular momentum distribution of the debris with the BH mass shown in Fig. 2.

In relativistic simulations the debris exhibits a positive shift in azimuthal angle relative to the Newtonian analogs which arises after $> 2\pi$ azimuthal rotation due to the apsidal advance of the orbit (Fig. 6). We compare the shifts measured from the MS1, MS2, and MS3 models with the orbital post-Newtonian (1PN) correction for apsidal advance,

$$\Delta\phi_p^{\rm PN} = 6\pi\frac{GM}{c^2 p}, \tag{4.1}$$

[51] where $p = R_p(1+e) \sim 2R_p$. From Fig. 5 we inspect the approximate periastron radii occupied by the bulk of the stellar debris (contours at the level $\Delta M/M_* \sim 10^{-1}$) in Newtonian simulations MS1, MS2, and MS3 as $R_p \sim 208M, 46M, 10M$, respectively. For these values of periastron radii the 1PN correction estimates apsidal advance of $\Delta\phi_p^{\rm PN} \sim 0.014\pi, 0.065\pi, 0.300\pi$. This is consistent with the shift measured between the debris in the Newtonian and relativistic simulations of 0.014π for MS1 (from 0.492π to 0.506π), 0.068π for MS2 (from 0.497π to 0.565π) and 0.396π for MS3 (from 0.498π to 0.894π). In comparing the Newtonian and relativistic result, we note a departure from the orbital 1PN correction for the apsidal advance of the

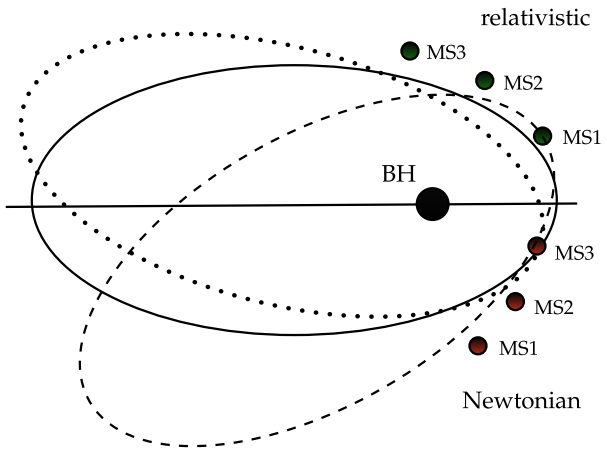

FIG. 6 (color online). Illustration of azimuthal locations of periastrons for orbits of bound debris elements after disruption (not to scale). In Newtonian simulations debris arrives to periastrons with the offset of $\lesssim 2\pi$ in azimuth (dotted line) relative to the periastron of the initial orbit (solid). In relativistic simulations debris arrives to periastrons with the offset of $> 2\pi$ in azimuth due to the apsidal advance of the orbit (dashed). The initial orbit is counterclockwise.

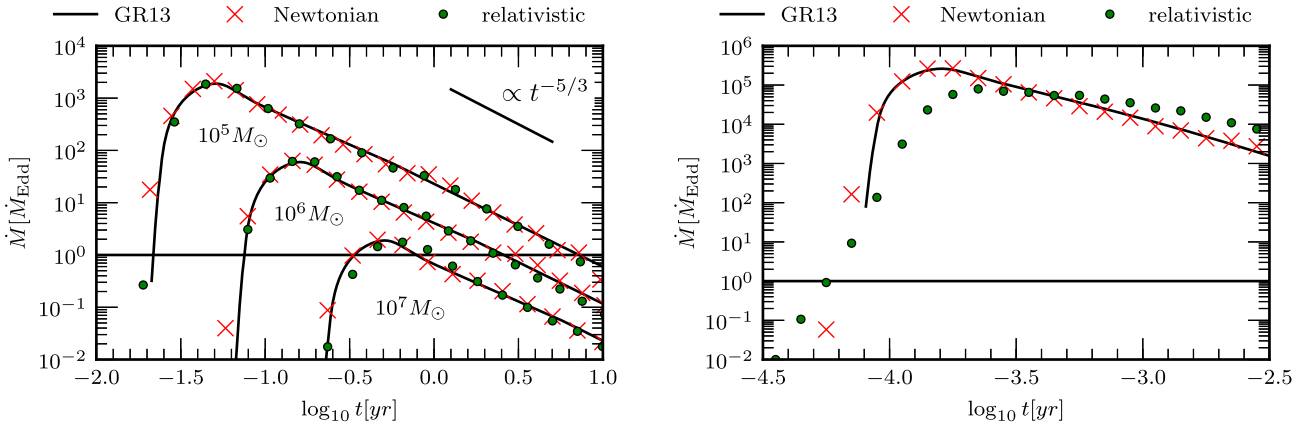

FIG. 7 (color online). Rates of return of the debris to periastrons as a function of time for MS1, MS2, MS3 (*left*) and WD models (*right*). Rates from Newtonian (red crosses) and relativistic simulations (green circles) are compared with parametric fits from [12] (solid black line).

bulk of debris as well as differences in the shape of the distribution for increasingly relativistic encounters. This indicates that the combined effects of the tide and star's trajectory contribute significantly to the apsidal advance in the relativistic encounters as well.

F. Relativistic effects in the return rate of debris

To calculate the rate of return of debris to the new periastrons, we construct a histogram in arrival time. In Fig. 7, we show the return rates for models MS1, MS2, MS3, and WD5 in units of $\dot{M}_{\rm Edd}$, where the Eddington luminosity is $L_{\rm Edd} = 1.3 \times 10^{38}\ {\rm erg\,s^{-1}}(M/M_\odot)$ and $\dot{M}_{\rm Edd} = L_{\rm Edd}/(0.1c^2)$ [52]. We compare results of Newtonian and relativistic simulations with fits based on Newtonian simulations by [12] (solid black line). In the left panel, we consider MS1, MS2, and MS3 encounters at the threshold of disruption ($\eta = 1$) and compare with $\beta = 1$ fits for disruption by $10^5, 10^6, 10^7 M_\odot$ BH. In the right panel, we consider a partial disruption of a white dwarf at $\eta = 1.44, \beta = 0.784$ and compare it with a $\beta = 0.8$ fit.

The return rate curves in all cases exhibit characteristic features similar to previous works that include a rise to the peak followed by a power law falloff. Closer inspection and comparison with the fits of [12] also reveal differences, which are somewhat visually attenuated due to the nature of the log-log plot. Newtonian rates exhibit a slight earlier rise than the fits (GR13) while relativistic rates show a more gradual rise to the peak. We interpret the differences between the Newtonian and relativistic rates as the result of the apsidal advance of the debris orbits from a combination of effects discussed in Sec. IV E.

We note that once debris leaves the computational domain, we are unable to account for the combined gravitational and hydrodynamical interaction with what remains in the computational domain. While this is the case, we note that this interaction between the streams and the core affects the least bound debris (which show up at later times in the return rate) more than the debris that is initially and supersonically stripped from the star close to periastron (which show up at early times in the return rate). We are also unable to account for the self-gravity of the tidal streams themselves. Nevertheless, we compare our estimate of the return rate with [12], who simulate the interaction between the core and the streams until the energy distribution reaches fixed values. The differences in Fig. 7 between our Newtonian simulations and those by [12] reflect the differences in how the orbital parameters of the debris are obtained from simulation as well as the evolution of the ballistic debris orbits. We note that these are small in comparison to the differences between the relativistic and Newtonian simulations.

For all simulations we measure the peak accretion rate ($\dot{M}_{\rm peak}$), the time when it occurs ($t_{\rm peak}$), as well as the power-law falloff (n^N_∞) and find that the values from our Newtonian simulations match well with the predictions of [12]. With the exception of the MS1 run, where relativistic effects are negligible, all other relativistic simulations exhibit noticeable differences with respect to their Newtonian counterparts. These are listed in Table II which in addition to already mentioned parameters shows the time for the return rate to reach the Eddington limit $t_{\rm Edd}$ and the shift in peak time $\Delta t_{\rm delay}$ between the Newtonian and relativistic simulations in days.

Table II and the right panel of Fig. 7 show that the return rate in relativistic simulation WD5, where apsidal advance is more severe, is suppressed by a factor of ~3 relative to the Newtonian rate. Along similar lines, the return rate curve in relativistic simulations is broadened and the occurrence of the peak in the return rate delayed. We attribute this delay to the apsidal advance of the orbits and the property of relativistic encounters to confine the energy and angular momentum distribution of the debris to a relatively narrow range of values. For example, we measure $\Delta t_{\rm delay}$ for the MS2 and MS3 models of about 6 and 23

TABLE II. Comparison of Newtonian and relativistic simulations. Peak return rate ($\dot{M}_{\rm peak}$), time when $\dot{M} = \dot{M}_{\rm Edd}$ ($t_{\rm Edd}$), time when $\dot{M} = \dot{M}_{\rm peak}$ ($t_{\rm peak}$), delay in peak time ($\Delta t_{\rm delay} = t^R_{\rm peak} - t^N_{\rm peak}$), power law index for the return rate from relativistic simulations (n^R_∞), and estimated BH mass ($M_{\rm est}$).

Label	$\dot{M}^N_{\rm peak}[\dot{M}_{\rm Edd}]$	$\dot{M}^R_{\rm peak}[\dot{M}_{\rm Edd}]$	$t^N_{\rm Edd}$[days]	$t^R_{\rm Edd}$[days]	$t^N_{\rm peak}$[days]	$t^R_{\rm peak}$[days]	$\Delta t_{\rm delay}$[days]	n^R_∞	$M_{\rm est}[M_\odot]$
MS1	2.1e + 03	2.2e + 03	7.1	7.6	1.9e + 01	1.9e + 01	0.0	−1.64	1.00e + 05
MS2	6.9e + 01	7.0e + 01	2.6e + 01	2.8e + 01	5.9e + 01	6.5e + 01	5.7	−1.66	1.17e + 06
MS3	2.2	1.8	1.2e + 02	1.4e + 02	1.9e + 02	2.1e + 02	2.3e + 01	−1.66	1.26e + 07
WD5	2.9e + 05	8.9e + 04	2.3e − 02	1.8e − 02	5.9e − 02	8.8e − 02	2.8e − 02	−1.61	3.10e + 05
WD6	1.1e + 05	2.9e + 05	2.9e − 02	2.9e − 02	6.3e − 02	1.0e − 01	3.7e − 02	−1.73	3.06e + 05

days, respectively. For the WD5 and WD6 models, which play out on much shorter time scales, the delays are only about ∼0.03–0.04 days. In the next section we discuss implications of the relativistic effects in the return rate curves in the context of observations and estimates of the BH mass.

V. DISCUSSION

Our simulations show that relativistic effects manifest in the return rate of the debris in two ways: they are noticeable in a more gradual rise of the return rate curve to the peak as well as in the delay of the peak rate relative to the Newtonian simulations. As expected, the magnitude of these effects increases for encounters that occur closer to the BH and while they are negligible in the MS1 model, they are present in MS2 and MS3 and fairly pronounced in the WD encounters. As relativistic effects are expected to affect the dynamics of the debris in these types of encounters, a pertinent question is *can they be detected in observations?*

In the previous section we quantify the importance of relativistic effects by calculating the "lead time" of the relativistic curves before the peak and the time delay of the peak relative to the Newtonian ones. Specifically, we measure the delay in the peak of the return rate of about 6 days and 23 days for encounters MS2 and MS3, respectively (Table II). In comparison, the typical cadence of images and photometry taken as a part of the Pan-STARRS1 Medium-Deep Field survey is every 3 nights [53]. Thus, these effects are in principle measurable with the current transient sky surveys if the ballistic return rate of the debris is proportional to the event light curve. This is an intriguing possibility, especially for the MS2 class of events, which have been considered numerous times in the literature as conventional Newtonian encounters. The relativistic effects in the return rate curve for WD encounters are even more severe, but may be difficult to measure with current surveys given the short time scale on which these events play out (< 1 day).

One important factor that prevents a simple interpretation of the return rates of the debris in terms of the observed light curves is the super-Eddington nature of the return rates. Namely, if simulated return rates (which determine the supply rate of the gas) are translated into the accretion rates onto the BH, they correspond to super-Eddington accretion rates. If these in turn power super-Eddington luminosities even for a brief period of time, radiative feedback is likely to strongly affect the dynamics of the accreting debris. That is, once the luminosity of the central source exceeds the Eddington limit, the portion of the light curve above this threshold (Fig. 7) will be shaped by the response of the debris to radiation pressure. As our simulations do not account for interactions of matter and radiation, we cannot determine whether signatures of relativistic effects will be preserved above this threshold.

We note that relativistic features in the early, sub-Eddington phase of evolution may still be preserved. In the early times of the rate, the relativistic curves have shallower slopes than the Newtonian counterparts. It is an interesting situation if an observed light curve from a relativistic encounter was unknowingly modeled by a light curve calculated from Newtonian simulations. In this case, the peaks of the two curves may be arbitrarily shifted along the time axis until they overlap but the slopes in the portion of the curves leading to the peak would be discrepant. We indeed find an indication of this behavior in the light curve of a tidal disruption event PS1-10jh for which the early rise in the light curve has been observed in the optical band with Pan-STARRS1 (see Fig. 2 in [28]). The exact nature of this tidal disruption event has been disputed and two different explanations have been offered in the literature. One group of authors, including the authors of this paper, suggests that this is a tidal disruption of a helium WD by a $\sim 10^6 M_\odot$ BH [28,54], while the other explains it in terms of the disruption of a main sequence star by a $\sim 10^7 M_\odot$ BH [55]. Both are in agreement that the encounter is likely to be relativistic. The case of PS1-10jh is interesting but unlikely to be constrained by further observations because the unique spectral and photometric features that can be used to infer its nature have faded out of sight. Thus, the only remaining prospect to understand this object may be through careful modeling of its relativistic light curve, which we defer to future work.

Given a possibility that relativistic features in the light curve of PS1-10jh have already been detected, it is of interest to consider what kind of biases can be introduced to interpretation of tidal disruption events if parametric fits based on Newtonian simulations are used to model light curves from relativistic encounters. We address this issue

by applying a simple model of the return rate curves from our relativistic simulations by Newtonian fits by [12]. We line up the relativistic and Newtonian curves in such way that their peaks overlap, as it would be the case with a majority of routines used to fit the observed data. Assuming a known structure of the disrupted star, the timing and magnitude of the peak are directly determined by the mass of the BH and strength of the encounter. Solving for these properties in practice allows an inference of the BH mass from tidal disruption events. Therefore, our simple modeling procedure provides estimates for the BH masses which we show in the last column of Table II as $M_{\rm est}$. Except for the MS1 run which does not exhibit significant relativistic effects, we find that a simple model of relativistic encounters with Newtonian parametric fit of the peak time leads to an overestimate of the BH mass by tens of percent in the case of disruptions of main sequence stars and a factor of few for WD disruptions. We nevertheless caution that more robust estimates of the BH mass require the development of proper data analysis tools, a worthwhile task that is out of the scope of this paper.

Given the increasing quality and detailed observational coverage of tidal disruption events a question of how debris circularizes to form an accretion disk becomes ever more pressing. In this paper we show that evolution in angular momentum is as important as the evolution in orbital energy of the debris and that the first step towards reconstruction of the debris orbits can be made only if both are known. An important consequence of this is shown in Fig. 4 where both bound and unbound fluid elements mix as they approach their periastrons. As this likely leads to orbit crossing and collisions, it has important implications for the evolution of debris disks. While we obtain the orbital map of the debris in the frame of the BH by propagating fluid elements semianalytically from the final snapshot of the simulation forward in time, this approach does not account for the effects of (magneto)hydrodynamics, self-gravity, or radiation transport. It thus does not provide a final answer about how debris disks evolve but it makes a point that angular momentum distribution as well as relativistic effects are likely to play an important role.

VI. CONCLUSIONS

In this paper, we used a suite of Newtonian and relativistic simulations of tidal disruption encounters of MS and WD stars with BHs to investigate relativistic effects in the dynamics of debris. We developed a local-to-BH frame transformation in order to calculate the orbital parameters of the debris and used these to infer the return rate of the debris as a function of time. We evaluate the relativistic effects in the orbital energy and angular momentum of the debris as a function of BH mass and stellar type. Severe relativistic effects lead to the mixing and collision of fluid elements that are both bound and unbound to the BH underlining the need for a full hydrodynamic treatment to accurately capture the evolution of debris accretion disks. The two most pronounced signatures of relativistic effects in the return rate of the debris to periastron are the gradual rise and offset in the peak of the curve relative to the Newtonian predictions. These are significant enough in the encounters of MS stars and BHs that they can in principle be measured by the current synoptic sky surveys, assuming that the return rate is proportional to the event light curve. Furthermore, with this assumption, if the tidal disruption light curve from a relativistic encounter is simply modeled with a Newtonian parametric fit of the peak time, this can lead to an overestimate in the BH mass by a factor of $\sim$few $\times$ 0.1 and $\sim$few for disruptions of the MS stars and WDs, respectively.

ACKNOWLEDGMENTS

R. M. C. thanks the anonymous referees for providing valuable queries for clarity. The authors are grateful to the Kavli Institute for Theoretical Physics for hosting the program, *A Universe of Black Holes*, where a portion of this work was completed. This research was supported in part by the National Science Foundation under Grants No. NSF PHY-1125915 and No. NSF AST-1333360. T. B. acknowledges the support from the Alfred P. Sloan Foundation under Grant No. BR2013-016.

APPENDIX A: EXPANSION COEFFICIENTS IN FNC-TO-BH FRAME TRANSFORMATION

The expansion coefficients ${\sigma_{ij}}^{\mu}$ and ${\kappa_{ijk}}^{\mu}$ in Eq. (3.5) and Eq. (3.6) are obtained by the following procedure [56]. The FNC frame center at $X^{\mu}_{(0)}$ is located on a timelike geodesic $\mathcal{G}$ parametrized by proper time τ in the BH frame. The relation between the Fermi normal coordinates and the tetrad on $\mathcal{G}$ may be expressed as the evaluation at $s = 1$ of the solution $X^{\mu}(s)$ of the initial value problem for a geodesic,

$$\frac{d^2X^{\mu}}{ds^2} + {\Gamma^{\mu}}_{\alpha\beta}\frac{dX^{\alpha}}{ds}\frac{dX^{\beta}}{ds} = 0,$$
$$X^{\mu}(0) = X^{\mu}_{(0)}, \qquad \frac{dX^{\mu}}{ds}(0) = x^i {\lambda_i}^{\mu}(\tau), \tag{A1}$$

for spatial components $i = 1, 2, 3$. From the initial conditions, we express the expansion for $X^{\mu}(s)$ as

$$X^{\mu}(s) = X^{\mu}_{(0)} + s a^{\mu}_1 + \frac{1}{2}s^2 a^{\mu}_2 + \frac{1}{6}s^3 a^{\mu}_3 + \cdots, \tag{A2}$$

where $a^{\mu}_1 = {\lambda_i}^{\mu} x^i$ and a_2, a_3, a_4, and a_5 are to be determined, and the connection coefficients are

$${\Gamma^{\mu}}_{\alpha\beta}(X^{\mu}(s)) = {\Gamma^{\mu}}_{\alpha\beta}|_0 + {\Gamma^{\mu}}_{\alpha\beta,\gamma}|_0 (X^{\gamma}(s) - X^{\gamma}_0) + \frac{1}{2}{\Gamma^{\mu}}_{\alpha\beta,\gamma\delta}|_0 (X^{\gamma}(s) - X^{\gamma}_0)(X^{\delta}(s) - X^{\delta}_0) + \cdots, \tag{A3}$$

with evaluations at $X^\mu_{(0)}$. Substituting Eq. (A2) and Eq. (A3) into the geodesic equation (A1) and comparing terms at each power of s, we have

$$\sigma_{ij}{}^{\mu} = -\Gamma^{\mu}{}_{\alpha\beta}|_0 \lambda_i{}^{\alpha}\lambda_j{}^{\beta}$$
$$\kappa_{ijk}{}^{\mu} = (2\Gamma^{\nu}{}_{\alpha\beta}\Gamma^{\mu}{}_{\nu\gamma} - \Gamma^{\mu}{}_{\alpha\beta,\gamma})|_0 \lambda_i{}^{\alpha}\lambda_j{}^{\beta}\lambda_k{}^{\gamma}. \quad \text{(A4)}$$

APPENDIX B: ORBITAL PARAMETERS OF THE DEBRIS

1. Newtonian gravitational potential

We consider the dynamics of the stellar debris in a Newtonian gravitational potential described by time t and spatial coordinates $X^i = \{r, \theta, \phi\}$ and velocities $V^i = dX^i/dt = \dot{X}^i$. For a general orbit in a Newtonian gravitational potential $\Phi_N = -M/r$ (in geometrized units), an equation relating the specific orbital energy ϵ and angular momentum ℓ is given by

$$\epsilon = -\frac{M}{r} + \frac{1}{2}\left(\dot{r}^2 + \frac{\ell^2 + \mathcal{Q}}{r^2}\right), \quad \text{(B1)}$$

where $\ell = r^2 \sin^2\theta\dot{\phi}$ and $\mathcal{Q} = \ell^2\cot^2\theta + r^4\dot{\theta}^2$ [41]. We parametrize the orbit in terms of the semilatus rectum p and eccentricity e with definitions for the turning points at periastron R_p and apastron R_a,

$$R_p = \frac{pM}{1+e}, \qquad R_a = \frac{pM}{1-e}. \quad \text{(B2)}$$

Substituting Eq. (B2) into Eq. (B1) at $\dot{r} = 0$, we relate the specific orbital energy and angular momentum with the semilatus rectum and eccentricity,

$$|\epsilon| = \frac{M(1-e^2)}{2p}, \qquad \ell = \sqrt{pM - \mathcal{Q}} \quad \text{(B3)}$$

or

$$pM = (\ell^2 + Q), \qquad eM = \sqrt{M^2 + 2\epsilon(\ell^2 + \mathcal{Q})}. \quad \text{(B4)}$$

Note that the semimajor axis a is related to these quantities by $a = (R_p + R_a)/2 = p/(1-e^2) = M/(2|\epsilon|)$.

The time evolution along the orbit is obtained by rewriting Eq. (B1) as

$$\frac{dt}{dr} = \sqrt{\frac{a}{M}}\frac{r}{\sqrt{a^2e^2 - (r-a)^2}}. \quad \text{(B5)}$$

We introduce a radial phase angle $\xi = [0, 2\pi]$ to parametrize the orbit [41],

$$r = a(1 - e\cos\xi). \quad \text{(B6)}$$

Substituting Eq. (B6) into Eq. (B5), we have a regularized equation for the time evolution,

$$\frac{dt}{d\xi} = \sqrt{\frac{a^3}{M}}(1 - e\cos\xi). \quad \text{(B7)}$$

We regularize the first-order equation of motion in θ [from $\mathcal{Q}$ in Eq. (B1)] in a similar manner to [57], by defining $\mathcal{Z} = \cos^2\theta$ and introducing a phase $\varphi = [0, 2\pi]$ such that $\mathcal{Z} = \mathcal{Z}_0\cos^2\varphi$. Turning points in θ occur at $\mathcal{Z}_0 = \mathcal{Q}/(\mathcal{Q} + \ell^2)$, where $\theta_\pm = \cos^{-1}(\pm\sqrt{\mathcal{Z}_0})$. We then have a first-order equation for φ,

$$\frac{d\varphi}{dt} = \frac{1}{r^2}\sqrt{\frac{\mathcal{Q} - \mathcal{Z}(\mathcal{Q} + \ell^2)}{\mathcal{Z}_0 - \mathcal{Z}}}, \quad \text{(B8)}$$

which parametrizes motion in $\theta = \cos^{-1}(\cos\varphi/\sqrt{\mathcal{Z}_0})$. Motion in ϕ is obtained in a straightforward manner by integrating the first-order equation from ℓ in Eq. (B1).

2. Schwarzschild spacetime

We consider the dynamics of the stellar debris in the spacetime of a Schwarzschild BH described by coordinates $X^\mu = (t, r, \theta, \phi)$, parametrized by proper time τ, and four-velocity $U^\mu = dX^\mu/d\tau = \dot{X}^\mu$. A relation for general orbits on Schwarzschild is given by

$$\epsilon^2 = \dot{r}^2 + f\left(1 + \frac{\ell^2 + \mathcal{Q}}{r^2}\right), \quad \text{(B9)}$$

in terms of the specific orbital energy $\epsilon = f\dot{t}$, specific angular momentum $\ell = r^2\sin^2\theta\dot{\phi}$, and Carter constant $\mathcal{Q} = \ell^2\cot^2\theta + r^4\dot{\theta}^2$, where $f = 1 - 2M/r$ [40].

Substituting Eq. (B2) into (B9), we relate the specific orbital energy and angular momentum with the semilatus rectum and eccentricity,

$$\epsilon^2 = \frac{(p-2-2e)(p-2+2e)}{p(p-3-e^2)},$$
$$\ell^2 = \frac{p^2M^2}{p-3-e^2} - \mathcal{Q}. \quad \text{(B10)}$$

Instead of inverting (B10) to obtain relations for $\{e, p\}$ in terms of given quantities $\{\epsilon, \ell\}$, we make use of the third root of the effective potential [42],

$$r_3 = \frac{2Mp}{p-4}. \quad \text{(B11)}$$

Given $\{\epsilon, \ell\}$, we numerically solve for this root with a Newton-Raphson method [58] within the interval $\{1.0M, 4.0M\}$ to obtain p from Eq. (B11). Using Eq. (B10), we obtain e and then R_p and R_a from Eq. (B2).

The orbital radius of the geodesic is parametrized by the radial phase angle χ,

$$r(\chi) = \frac{pM}{1 + e\cos\chi}. \tag{B12}$$

The evolution along the orbit in Schwarzschild time is given by [42]

$$\frac{dt}{d\chi} = \frac{p^2 M}{(p - 2 - 2e\cos\chi)(1 + e\cos\chi)^2} \times \left[\frac{(p-2)^2 - 4e^2}{p - 6 - 2e\cos\chi}\right]^{1/2}. \tag{B13}$$

Motion in θ and ϕ is obtained similarly to the Newtonian case.

[1] M. J. Rees, Nature (London) **333**, 523 (1988).
[2] E. S. Phinney, in *The Center of the Galaxy: Proceedings of the 136th Symposium of the International Astronomical Union, Los Angeles, U.S.A., 1988*, edited by M. Morris (Kluwer Academic Publishers, Dordrecht, 1988), p. 543.
[3] C. R. Evans and C. S. Kochanek, Astrophys. J. Lett. **346**, L13 (1989).
[4] N. Bade, S. Komossa, and M. Dahlem, Astron. Astrophys. **309**, L35 (1996).
[5] D. Grupe, H.-C. Thomas, and K. M. Leighly, Astron. Astrophys. **350**, L31 (1999).
[6] S. Komossa and J. Greiner, Astron. Astrophys. **349**, L45 (1999).
[7] J. Greiner, R. Schwarz, S. Zharikov, and M. Orio, Astron. Astrophys. **362**, L25 (2000).
[8] J. L. Donley, W. N. Brandt, M. Eracleous, and T. Boller, Astron. J. **124**, 1308 (2002).
[9] S. Komossa, J. Halpern, N. Schartel, G. Hasinger, M. Santos-Lleo, and P. Predehl, Astrophys. J. Lett. **603**, L17 (2004).
[10] J. P. Halpern, S. Gezari, and S. Komossa, Astrophys. J. **604**, 572 (2004).
[11] G. Lodato, A. R. King, and J. E. Pringle, Mon. Not. R. Astron. Soc. **392**, 332 (2009).
[12] J. Guillochon and E. Ramirez-Ruiz, Astrophys. J. **767**, 25 (2013).
[13] K. Hayasaki, N. Stone, and A. Loeb, Mon. Not. R. Astron. Soc. **434**, 909 (2013).
[14] L. Dai, A. Escala, and P. Coppi, Astrophys. J. Lett. **775**, L9 (2013).
[15] A. Loeb and A. Ulmer, Astrophys. J. **489**, 573 (1997).
[16] A. Ulmer, Astrophys. J. **514**, 180 (1999).
[17] L. E. Strubbe and E. Quataert, Mon. Not. R. Astron. Soc. **400**, 2070 (2009).
[18] L. E. Strubbe and E. Quataert, Mon. Not. R. Astron. Soc. **415**, 168 (2011).
[19] G. Lodato and E. Rossi, Mon. Not. R. Astron. Soc. **410**, 359 (2011).
[20] M. Kesden, Phys. Rev. D **86**, 064026 (2012).
[21] R. Haas, R. V. Shcherbakov, T. Bode, and P. Laguna, Astrophys. J. **749**, 117 (2012).
[22] W. E. East and F. Pretorius, Phys. Rev. D **87**, 101502 (2013).
[23] S. van Velzen, G. R. Farrar, S. Gezari, N. Morrell, D. Zaritsky, L. Östman, M. Smith, J. Gelfand, and A. J. Drake, Astrophys. J. **741**, 73 (2011).
[24] J. S. Bloom *et al.*, Science **333**, 203 (2011).
[25] A. J. Levan *et al.*, Science **333**, 199 (2011).
[26] D. N. Burrows *et al.*, Nature (London) **476**, 421 (2011).
[27] S. B. Cenko *et al.*, Mon. Not. R. Astron. Soc. **420**, 2684 (2012).
[28] S. Gezari *et al.*, Nature (London) **485**, 217 (2012).
[29] J. Camp, S. Barthelmy, L. Blackburn, K. G. Carpenter, N. Gehrels, J. Kanner, F. E. Marshall, J. L. Racusin, and T. Sakamoto, Exp. Astron. **36**, 505 (2013).
[30] J. Kanner, J. Baker, L. Blackburn, J. Camp, K. Mooley, R. Mushotzky, and A. Ptak, Astrophys. J. **774**, 63 (2013).
[31] R. Chornock *et al.*, Astrophys. J. **780**, 44 (2014).
[32] I. Arcavi *et al.*, arXiv:1405.1415 [astro-ph.HE].
[33] T. W.-S. Holoien, J. L. Prieto, D. Bersier, C. S. Kochanek, K. Z. Stanek, B. J. Shappee, D. Grupe, U. Basu, J. F. Beacom, J. Brimacombe, J. S. Brown, A. B. Davis, J. Jencson, G. Pojmanski, and D. M. Szczygiel, arXiv:1405.1417.
[34] S. Rosswog, E. Ramirez-Ruiz, and W. R. Hix, Astrophys. J. **695**, 404 (2009).
[35] R. V. Shcherbakov, A. Pe'er, C. S. Reynolds, R. Haas, T. Bode, and P. Laguna, Astrophys. J. **769**, 85 (2013).
[36] M. MacLeod, J. Goldstein, E. Ramirez-Ruiz, J. Guillochon, and J. Samsing, arXiv:1405.1426 [astro-ph.HE].
[37] R. M. Cheng and C. R. Evans, Phys. Rev. D **87**, 104010 (2013).
[38] W. H. Press and S. A. Teukolsky, Astrophys. J. **213**, 183 (1977).
[39] N. Stone, R. Sari, and A. Loeb, Mon. Not. R. Astron. Soc. **435**, 1809 (2013).
[40] C. Misner, K. Thorne, and J. Wheeler, *Gravitation* (W.H. Freeman, San Francisco, 1973).
[41] L. D. Landau and E. M. Lifshitz, *Mechanics* (Pergamon, New York, 1969).
[42] C. Cutler, D. Kennefick, and E. Poisson, Phys. Rev. D **50**, 3816 (1994).
[43] M. Ishii, M. Shibata, and Y. Mino, Phys. Rev. D **71**, 044017 (2005).
[44] V. P. Frolov, A. M. Khokhlov, I. D. Novikov, and C. J. Pethick, Astrophys. J. **432**, 680 (1994).
[45] S. Kobayashi, P. Laguna, E. S. Phinney, and P. Mészáros, Astrophys. J. **615**, 855 (2004).
[46] Z. B. Etienne, J. A. Faber, Y. T. Liu, S. L. Shapiro, K. Taniguchi, and T. W. Baumgarte, Phys. Rev. D **77**, 084002 (2008).
[47] L. F. Roberts, D. Kasen, W. H. Lee, and E. Ramirez-Ruiz, Astrophys. J. Lett. **736**, L21 (2011).

[48] F. Foucart, M. D. Duez, L. E. Kidder, M. A. Scheel, B. Szilagyi, and S. A. Teukolsky, Phys. Rev. D **85**, 044015 (2012).
[49] W. E. East, F. Pretorius, and B. C. Stephens, Phys. Rev. D **85**, 124009 (2012).
[50] K. Kyutoku, K. Ioka, and M. Shibata, Phys. Rev. D **88**, 041503 (2013).
[51] S. Weinberg, *Gravitation and Cosmology: Principles and Applications of the General Theory of Relativity* (Wiley, New York, 1972).
[52] S. L. Shapiro and S. A. Teukolsky, *Black Holes, White Dwarfs, and Neutron Stars: The Physics of Compact Objects* (Wiley, New York, 1983).
[53] N. Kaiser, W. Burgett, K. Chambers, L. Denneau, J. Heasley, R. Jedicke, E. Magnier, J. Morgan, P. Onaka, and J. Tonry, in *Society of Photo-Optical Instrumentation Engineers (SPIE) Conference Series*, Society of Photo-Optical Instrumentation Engineers (SPIE) Conference Series (SPIE, 2010), Vol. 7733.
[54] T. Bogdanović, R. M. Cheng, and P. Amaro-Seoane, Astrophys. J. **788**, 99 (2014).
[55] J. Guillochon, H. Manukian, and E. Ramirez-Ruiz, Astrophys. J. **783**, 23 (2014).
[56] D. Klein and P. Collas, Classical Quantum Gravity **25**, 145019 (2008).
[57] S. A. Hughes, Phys. Rev. D **64**, 064004 (2001).
[58] W. H. Press, B. P. Flannery, and S. A. Teukolsky, *Numerical Recipes. The Art of Scientific Computing* (Cambridge University Press, Cambridge, England, 1986).